ISSN 1029-9599, Physical Mesomechanics, 2017, Vol. 20, No. 3, pp. 311–323. © Pleiades Publishing, Ltd., 2017.
Original Text © M. Diehl, D. An, P. Shanthraj, S. Zaefferer, F. Roters, D. Raabe, 2017, published in Fizicheskaya Mezomekhanika, 2017, Vol. 20, No. 3, pp. 69–80.

Crystal Plasticity Study on Stress and Strain Partitioning in a Measured 3D Dual Phase Steel Microstructure

M. Diehl*, D. An, P. Shanthraj, S. Zaefferer, F. Roters, and D. Raabe

Max-Planck-Institut für Eisenforschung GmbH, Düsseldorf, 40237 Germany
** e-mail: m.diehl@mpie.de*

Received January 24, 2017

Abstract—Dual phase steels are advanced high strength alloys typically used for structural parts and reinforcements in car bodies. Their good combination of strength and ductility and their lean composition render them an economically competitive option for realizing multiple lightweight design options in automotive engineering. The mechanical response of dual phase steels is the result of the strain and stress partitioning among the ferritic and martensitic phases and the individual crystallographic grains and subgrains of these phases. Therefore, understanding how these microstructural features influence the global and local mechanical properties is of utmost importance for the design of improved dual phase steel grades. While multiple corresponding simulation studies have been dedicated to the investigation of dual phase steel micromechanics, numerical tools and experiment techniques for characterizing and simulating real 3D microstructures of such complex materials have been emerged only recently. Here we present a crystal plasticity simulation study based on a 3D dual phase microstructure which is obtained by EBSD tomography, also referred to as 3D EBSD (EBSD—electron backscatter diffraction). In the present case we utilized a 3D EBSD serial sectioning approach based on mechanical polishing. Moreover, sections of the 3D microstructure are used as 2D models to study the effect of this simplification on the stress and strain distribution. The simulations are conducted using a phenomenological crystal plasticity model and a spectral method approach implemented in the Düsseldorf Advanced Material Simulation Kit (DAMASK).

DOI: 10.1134/S1029959917030079

Keywords: crystal plasticity, dual phase steel, microstructure, DAMASK, spectral method, 3D EBSD

1. INTRODUCTION

Dual phase steels, consisting of a relatively soft ferritic matrix reinforced by strong martensitic islands, are frequently used for structural parts and reinforcements in car bodies. Their good combination of strength and ductility is a result of the strain and stress partitioning among these two different phases and the individual crystallographic grains and subgrains [1]. Therefore, understanding how these microstructural features influence the global mechanical properties is of very high importance for the design of improved dual phase steel grades. Hence, a large number of simulation studies—starting with Karlsson and Sundström [2] in 1974—has been dedicated to the investigation of dual phase steel micromechanics. However, even recent (crystal plasticity) simulations aiming at a better understanding of dual phase steel micromechanics are often performed on models that are significantly simplified representations of the microstructure: Either (a) 2D microstructures obtained from measurements of grain morphology and crystallographic orientation [3–5] or (b) idealized 3D microstructures without crystallographic orientation information [6–10] and/or simplified grain morphology, phase distribution, and orientation scatter [7, 8, 11–13] are used. Both approaches have their drawbacks: Simulations using 2D microstructures reduce real materials to artificially extruded, hence columnar materials and thus leave out a significant part of the grain and phase neighborhood, imposing local boundary conditions that are quantitatively and qualitatively different than in a 3D situation [12, 14, 15]. Simplified structures obviously miss details associated with grain morphology, martensite distribution, phase and texture percolation effects, and in-grain crystallogra-

phic orientation scatter present in real dual phase microstructures.[1] In the present study we, therefore, investigate the micromechanical behavior of a measured 3D dual phase microstructure to overcome these limitations. Moreover, sections of the 3D microstructure are used in the form of extruded 2D models to study how the reduction of a 3D microstructure into a 2D one influences the stress and strain distribution.

The study is structured as follows: Fist, the crystal plasticity model and the numerical method for solving the mechanical boundary value problem are presented. Afterwards, details of the microstructure model—starting from the experimental characterization—are given, followed by the presentation and discussion of the results. The study finishes with concluding remarks and an outlook on further work.

2. SIMULATION FRAMEWORK

The simulations presented in this work are performed by using the Düsseldorf Advanced Material Simulation Kit (DAMASK) available as free and open source software on https://damask.mpie.de [16]. In DAMASK, crystal plasticity is modeled within a continuum mechanics approach by taking into account the distinct deformation modes of crystalline matter. The details of the underlying continuum mechanics description, the crystal plasticity formulation, and the numerical technique to solve the boundary value problem for static mechanical equilibrium are presented in the following.

2.1. Continuum Mechanical Description

$\mathcal{B}$ denotes a body that occupies the region $\mathcal{B}_0$ in the reference configuration and $\mathcal{B}_t$ in the current configuration. The location of the material points in the reference state is given by $\mathbf{x}$, $\mathbf{x} \in \mathcal{B}_0$ and in a deformed configuration by $\mathbf{y}$, $\mathbf{y} \in \mathcal{B}_t$.

A deformation map $\boldsymbol{\chi}(\mathbf{x})$: $\mathbf{x} \in \mathcal{B}_0 \rightarrow \mathbf{y} \in \mathcal{B}_t$ maps points $\mathbf{x}$ in the reference configuration to points $\mathbf{y}$ in the current configuration. The displacement $\mathbf{u}$ of a material point is the difference vector between these configurations:

$$\mathbf{u}(\mathbf{x}, t) = \boldsymbol{\chi}(\mathbf{x}, t) - \mathbf{x}. \tag{1}$$

Focusing on a point in time, i.e. a fixed deformation state, allows simplifying the notation to $\mathbf{u}(\mathbf{x}) = \boldsymbol{\chi}(\mathbf{x}) - \mathbf{x}$.

A line segment d$\mathbf{x}$ in an infinitesimal neighborhood of a material point $\mathbf{x}$ is pushed forward by

$$\mathbf{y} + \mathrm{d}\mathbf{y} = \mathbf{y} + \frac{\partial \mathbf{y}}{\partial \mathbf{x}} \mathrm{d}\mathbf{x} + \mathcal{O}(\mathrm{d}\mathbf{x}^2). \tag{2}$$

Neglecting terms of higher order, d$\mathbf{y}$ can be expressed as

$$\mathrm{d}\mathbf{y} = \frac{\partial \mathbf{y}}{\partial \mathbf{x}} \mathrm{d}\mathbf{x} = \frac{\partial \boldsymbol{\chi}(\mathbf{x})}{\partial \mathbf{x}} \mathrm{d}\mathbf{x} = \underbrace{\nabla \boldsymbol{\chi}}_{=:\mathbf{F}(\mathbf{x})} \mathrm{d}\mathbf{x}, \tag{3}$$

where $\mathbf{F}(\mathbf{x})$ is the deformation gradient and ∇ is the "del" operator. The deformation gradient maps the vector d$\mathbf{x}$ at $\mathbf{x}$ in the reference configuration to the vector d$\mathbf{y}$ at $\mathbf{y}$ in the current configuration.

For a moving body, the position of the material points varies with time. The material velocity field is defined as[2]

$$\mathbf{v} = \frac{\mathrm{d}\mathbf{u}(\mathbf{x})}{\mathrm{d}t} = \dot{\mathbf{u}} = \dot{\boldsymbol{\chi}}. \tag{4}$$

$\dot{\mathbf{u}} = \dot{\boldsymbol{\chi}}$ holds because the points in the reference configuration do not change their position, i.e. $\mathrm{d}\mathbf{x}/\mathrm{d}t = \mathbf{0}$. The spatial gradient of the velocity field is

$$\mathbf{L} = \frac{\partial \mathbf{v}}{\partial \mathbf{y}}, \tag{5}$$

where $\mathbf{L}$ is called the velocity gradient. Using the chain rule, it can be expressed as

$$\mathbf{L} = \dot{\mathbf{F}} \cdot \mathbf{F}^{-1}. \tag{6}$$

2.2. Crystal Plasticity Formulation

As common in large-strain crystal plasticity modeling, the deformation gradient $\mathbf{F}$ is multiplicatively split up [17] into an elastic part $\mathbf{F}_e$ and a plastic part $\mathbf{F}_p$ as

$$\mathbf{F} = \mathbf{F}_e \mathbf{F}_p \tag{7}$$

to model the combined elastic-plastic response usually seen in metals.

For small strains (and short loading times), the behaviour is usually purely elastic, i.e. reversible and linear (Hookean) elasticity can be assumed. Therefore, the second Piola–Kirchhoff stress $\mathbf{S}$ depends on the elastic Green–Lagrange strain via the anisotropic elastic stiffness $\mathbb{C}$. This relation is written in an artificial, only elastically deformed "intermediate configuration"[3] [17]:

$$\mathbf{S} = \mathbb{C}(\mathbf{F}_e^{\mathrm{T}} \mathbf{F}_p - \mathbf{I})/2. \tag{8}$$

[1] A recent example that shows how most of these features can be included into artificial microstructures is given by Pagenkopf et al. [13].

[2] To simplify the notation, in the following, the argument $\mathbf{x}$ is dropped whenever it is possible, i.e. $\mathbf{F}(\mathbf{x})$ is denoted as $\mathbf{F}$ only.

[3] This is formally equivalent to the stress–strain relation in the reference configuration. The given relation is therefore a valid approximation for small elastic strains, where the difference between reference and intermediate configuration is negligible.

Since $\mathbb{C}$ relates two symmetric tensors, it is itself symmetric and can be written as a 6×6 matrix.

The stress **S** is acting as a driving force for the plastic velocity gradient $\mathbf{L}_\mathrm{p}$. $\mathbf{L}_\mathrm{p}$ depends on the underlying microstructure represented by a state variable vector ξ of the plasticity model and possibly other variables:

$$\mathbf{L}_\mathrm{p} = \mathbf{f}(\mathbf{S}, \xi, ...) \tag{9}$$

with **f** depending on the details of the used plasticity model which might by sensitive to strain rate, temperature, etc. as indicated by "...".

From Eq. (6) follows

$$\dot{\mathbf{F}}_\mathrm{p} = \mathbf{L}_\mathrm{p}\mathbf{F}_\mathrm{p} \tag{10}$$

for the evolution of the plastic deformation gradient.

The set of nonlinear Eqs. (7) to (10) needs to be solved iteratively. In DAMASK, a Newton–Raphson scheme is employed for that. More details about the implementation are given by Kords [19].

The core of each crystal plasticity model is the formulation shown in Eq. (9). In this equation, the plastic deformation of the material and its dependence to the aforementioned influences are incorporated. For the evolution of the state ξ a crystal plasticity model needs to be completed by a second equation:

$$\dot{\xi} = \mathbf{g}(\mathbf{S}, \xi, ...). \tag{11}$$

The two integration schemes are performed staggered, i.e. Eqs. (7) to (10) are solved at a fixed plastic state, followed by a state update, the solution of Eqs. (7) to (10), and so forth until a converged solution is achieved within the tolerance limits specified.

Using **P** = **F S** for conversion from **S** to **P**, a crystal plasticity model (i.e. Eqs. (7) to (10)) can be summarized as

$$\mathbf{P}(\mathbf{x}) = \mathbf{f}(\mathbf{x}, \mathbf{F}, \xi, ...) \tag{12}$$

which is a stress–strain relation with dependence on the material state and model dependent parameters (denoted by "..." in Eq. (12)) such as loading rate and temperature.

The crystal plasticity model used in this study is based on a phenomenological description proposed by Hutchinson [20] for face-centered cubic (fcc) crystals. Here, it has been adopted for describing the behavior of body-centered cubic (bcc) crystallites. This model is based on the assumption that plastic deformation occurs on a slip system when the resolved shear stress exceeds a critical value.

The microstructural state is parameterized in terms of resistances ξ on $N_\mathrm{s} = 24$ slip systems of which 12 have a {110} and another 12 have a {112} plane. On both families of slip planes ⟨111⟩ directions are densely packed and serve as slip directions. The resistances on the $k = 1, ..., N_\mathrm{s}$ slip systems evolve from their initial value ξ_0 asymptotically to a system-dependent saturation value ξ_∞ with shear γ^m on all slip systems according to the relationship

$$\dot{\xi}^k = h_0 \sum_{m=1}^{N_\mathrm{s}} |\dot{\gamma}^m| \left|1 - \frac{\xi^m}{\xi_\infty^m}\right| \mathrm{sgn}\left(1 - \frac{\xi^m}{\xi_\infty^m}\right) h_{km}, \tag{13}$$

where h_{km} is an interaction matrix and h_0 and a are system dependent fitting parameters.

Given a set of current slip resistances, a slip system shears with a rate

$$\dot{\gamma}^k = \dot{\gamma}_0 \left|\frac{\tau^k}{\xi^k}\right|^n \mathrm{sgn}\tau^k, \tag{14}$$

with $\tau^k = \mathbf{S} \cdot (\mathbf{s}^k \otimes \mathbf{n}^k)$ being (according to Schmids law [21]) the resolved shear stress for applied stress **S** and the unit vectors along the slip direction $\mathbf{s}^k$ and along the slip plane normal $\mathbf{n}^k$. Non-Schmid contributions [22] are not taken into account.

The sum of shear rates on all systems determines finally the plastic velocity gradient

$$\mathbf{L}_\mathrm{p} = \sum_{k=1}^{N_\mathrm{s}} \dot{\gamma}^k \mathbf{s}^k \otimes \mathbf{n}^k. \tag{15}$$

2.3. Boundary Value Solver

For general cases, the solution for (static) equilibrium and strain compatibility under the given boundary conditions has to be sought numerically. A variety of numerical techniques exist for solving the differential equations. Most often, the finite element method is used. As an alternative solver, a spectral method using fast Fourier transforms was introduced by Moulinec and Suquet [23] in the field of material micromechanics and has gained significant attention during the last years [24–26]. Limited to periodic boundary conditions, this technique usually exceeds the finite element method in terms of solution quality because it uses trigonometric polynomials as ansatz functions. Moreover, since it operates in Fourier space, the use of fast Fourier transforms allows for a very time- and memory-efficient iterative solution algorithm. Various improvements and extensions were reported in the recent years: Lebensohn [27] extended it to the context of crystal viscoplasticity and showed the capabilities of this approach as well as several applications in a number of studies [28–30]. Crystal plasticity-based constitutive laws have also been successfully employed by, e.g., Suquet et al. [31] and Grennerat et al. [32].

Simulations of heterogeneous materials, however, are limited by the slow convergence of the original fixed-point iterative method when it is applied to materials with a large contrast in the local stiffness [33]. Several approaches have been proposed to overcome this limitation. Accelerated schemes have been introduced by Eyre and Milton [34] and Monchiet and Bonnet [35] for materials with large property contrasts. Michel et al. [33] suggested a method based on augmented Lagrangians that also works in the case of materials with infinite property contrast. Using the original formulation and substituting the fixed-point method by advanced solution methods is another option to improve convergence as shown by Zeman et al. [36] and Brisard and Dormieux [37].

The spectral formulation used in this study is the one presented by Eisenlohr et al. [38] and its extension by Shanthraj et al. [39]. Since the reader might not be familiar with this method, we outline it briefly in the following.

2.4. Formulation

The deformation map $\boldsymbol{\chi}(\mathbf{x})$ is expressed as a sum of a homogeneous deformation, characterized by a constant deformation gradient $\bar{\mathbf{F}}$, and a superimposed deformation fluctuation field $\tilde{\mathbf{w}}$:

$$\boldsymbol{\chi}(\mathbf{x}) = \bar{\mathbf{F}}\mathbf{x} + \tilde{\mathbf{w}}(\mathbf{x}), \tag{16}$$

for which periodicity conditions hold, i.e. $\tilde{\mathbf{w}}^- = \tilde{\mathbf{w}}^+$ on corresponding surfaces $\partial\mathcal{B}^-$ and $\partial\mathcal{B}^+$ on $\mathcal{B}$.

Equation (16) allows writing the deformation gradient **F** as the sum of a spatially homogeneous deformation part $\bar{\mathbf{F}}$ and a locally fluctuating displacement part $\tilde{\mathbf{F}}$:

$$\mathbf{F} = \bar{\mathbf{F}} + \tilde{\mathbf{F}}. \tag{17}$$

The material response, Eq. (12), is formally written as a relation between the deformation gradient **F** and the first Piola–Kirchhoff stress **P** through a strain energy density functional $\mathcal{W}$:

$$\mathbf{P}(\mathbf{x}) = \frac{\delta\mathcal{W}}{\delta\mathbf{F}(\mathbf{x})} = \mathbf{f}(\mathbf{x}, \mathbf{F}, \xi, ...). \tag{18}$$

2.5. Direct Variational Formulation

The direct variational formulation is closely related to the original spectral method suggested by Moulinec and Suquet [23] and the corresponding large-strain formulation introduced by Lahellec et al. [40] and Eisenlohr et al. [38]. Here it is written in a general form that allows replacing the original fixed-point approach by more powerful numerical solvers [39].

The equilibrated deformation field is obtained by minimizing $\mathcal{W}$ over all deformation fields that fulfill Eq. (16) for an externally prescribed average deformation. Static equilibrium expressed in real and Fourier[1] space follows as

$$\min_{\boldsymbol{\chi}} \mathcal{W} \Rightarrow \nabla \cdot \mathbf{P}(\mathbf{x}) = F^{-1}[\mathbf{P}(\mathbf{k})i\mathbf{k}] = \mathbf{0}, \tag{19}$$

which is equivalent to finding the root of the residual body force field

$$\mathcal{F}[\boldsymbol{\chi}(\mathbf{k})] \coloneqq \mathbf{P}(\mathbf{k})i\mathbf{k} = \mathbf{0}. \tag{20}$$

The differential Eq. (20) in Fourier space is numerically difficult to solve because of its high condition number. Introducing, in the spirit of Eshelby and Mura [41], a linear comparison material of stiffness $\mathbb{D}$ allows reformulation of Eq. (20) into an equivalent problem $\mathbf{P}(\mathbf{x}) = \mathbb{D}\mathbf{F}(\mathbf{x}) = \mathbb{D}\nabla\boldsymbol{\chi}$ with better numerical properties, i.e. a lower condition number. Equilibrium in this reference material is fulfilled if, for a given deformation map $\boldsymbol{\chi}$, the residual body force field vanishes

$$\mathcal{P}[\boldsymbol{\chi}(\mathbf{k})] \coloneqq \mathbb{D}[\boldsymbol{\chi}(\mathbf{k}) \otimes i\mathbf{k}]i\mathbf{k} = \mathbf{A}(\mathbf{k})\boldsymbol{\chi}(\mathbf{k}) = \mathbf{0}. \tag{21}$$

The acoustic tensor $\mathbf{A}(\mathbf{k})$ is a shorthand notation for $\mathbf{A}(\mathbf{k})\,\mathbf{a}(\mathbf{k}) \coloneqq \mathbb{D}[\mathbf{a}(\mathbf{k}) \otimes i\mathbf{k}]i\mathbf{k}$ for any given vector field $\mathbf{a}(\mathbf{k})$. It corresponds to an operator on a deformation map producing the body forces resulting in the reference material. The inverse $\mathbf{A}^{-1}$ therefore gives the deformation map that would result from a known body force field in the reference material. This deformation map vanishes if the body force field vanishes, i.e., in static equilibrium for a positive-definite $\mathbb{D}$. Next, an operator that results in the deformation map causing the same body force field in the reference material as a given deformation map in the original material is defined. This corresponds to a preconditioning operation of $\mathcal{P}^{-1}$ on the nonlinear operator $\mathcal{F}$. $\mathcal{P}$ is straightforward to invert since it is local in $\mathbf{k}$, with $\mathcal{P}^{-1} = \mathbf{A}(\mathbf{k})^{-1}$. The preconditioned system thus reads $(\forall \mathbf{k} \neq \mathbf{0})$:

$$\mathcal{P}^{-1}\mathcal{F}(\boldsymbol{\chi}(\mathbf{k})) = \mathbf{A}(\mathbf{k})^{-1}\mathbf{P}(\mathbf{k})i\mathbf{k} = \mathbf{0}. \tag{22}$$

The deformation gradient field corresponding to this deformation map is obtained from the gradient in real space of Eq. (22)

$$\mathcal{P}^{-1}\mathcal{F}[\boldsymbol{\chi}(\mathbf{k})] \otimes i\mathbf{k} = [\mathbf{A}(\mathbf{k})^{-1}\mathbf{P}(\mathbf{k})i\mathbf{k}] \otimes i\mathbf{k} = \mathbf{0}. \tag{23}$$

This is equivalent to Eq. (22) except for a constant residual field, i.e. at $\mathbf{k} = \mathbf{0}$ where the prescribed average deformation gradient is known to hold. Expressed

[1] Quantities in real space and Fourier space are distinguished by notation $\mathbf{Q}(\mathbf{x})$ and $\mathbf{Q}(\mathbf{k})$, respectively, with $\mathbf{x}$ the position in real space, $\mathbf{k}$ the frequency vector in Fourier space, and $i^2 = -1$. $F^{-1}[.]$ denotes the inverse Fourier transform.

in terms of the deformation gradient field, Eq. (23) reads

$$\mathcal{F}_{\mathrm{dir}}[\mathbf{F}(\mathbf{k})] := \boldsymbol{\Gamma}(\mathbf{k})\mathbf{P}(\mathbf{k}) = \mathbf{0}, \tag{24}$$

where the Gamma operator $\boldsymbol{\Gamma}(\mathbf{k})$ is defined as a shorthand notation to $\boldsymbol{\Gamma}(\mathbf{k})\mathbf{T}(\mathbf{k}) := [\mathbf{A}(\mathbf{k})^{-1}\mathbf{T}(\mathbf{k})i\mathbf{k}] \otimes i\mathbf{k}$ for a tensor field $\mathbf{T}(\mathbf{k})$.

2.6. Mixed Variational Formulation

The idea of using a mixed variational formulation was firstly outlined by Michel et al. [42] to overcome convergence problems with high phase contrast. Here, this idea is presented in a general form given by Shanthraj et al. [39]. In this formulation the equilibrium deformation field is obtained by minimizing $\mathcal{W}$ over all deformation gradient fields fulfilling Eq. (16) for an externally prescribed average deformation. Unlike in the direct variational formulation, the compatibility of the deformation gradient $\nabla \times \mathbf{F} = \mathbf{0}$, field is imposed as an auxiliary constraint

$$\min_{\mathbf{F}} \mathcal{W}(\mathbf{F}) \text{ subject to } \mathbf{F} = \nabla\boldsymbol{\chi}. \tag{25}$$

This can be reformulated as an unconstrained optimization problem by introducing a Lagrange multiplier field $\boldsymbol{\Lambda}(\mathbf{x})$, and a penalty term. Conveniently, the reference stiffness $\mathbb{D}$ as defined above is used as the penalty parameter. The resulting augmented Lagrange multiplier functional reads

$$\mathcal{L}[\mathbf{F}, \boldsymbol{\chi}, \boldsymbol{\Lambda}] = \mathcal{W} + \int_{\mathcal{B}_0} \boldsymbol{\Lambda}(\mathbf{x}) \cdot [\nabla\boldsymbol{\chi}(\mathbf{x}) - \mathbf{F}(\mathbf{x})] \mathrm{d}\mathbf{x} + \int_{\mathcal{B}_0} \frac{[\nabla\boldsymbol{\chi}(\mathbf{x}) - \mathbf{F}(\mathbf{x})] \cdot \mathbb{D}[\nabla\boldsymbol{\chi}(\mathbf{x}) - \mathbf{F}(\mathbf{x})]}{2} \mathrm{d}\mathbf{x}. \tag{26}$$

The equilibrium condition is equivalent to the saddle point of Eq. (26) (for details see [43]). This results in the following three stationary conditions:

$$\frac{\delta\mathcal{L}}{\delta\mathbf{F}(\mathbf{x})} = \mathbf{P}(\mathbf{x}) - \boldsymbol{\Lambda}(\mathbf{x}) + \mathbb{D}\{\mathbf{F}(\mathbf{x}) - \nabla\boldsymbol{\chi}(\mathbf{x})\} = \mathbf{0},$$
$$\frac{\delta\mathcal{L}}{\delta\boldsymbol{\chi}(\mathbf{x})} = \nabla[\boldsymbol{\Lambda}(\mathbf{x}) - \mathbb{D}\{\mathbf{F}(\mathbf{x}) - \nabla\boldsymbol{\chi}(\mathbf{x})\}] = \mathbf{0}, \tag{27}$$
$$\frac{\delta\mathcal{L}}{\delta\boldsymbol{\Lambda}(\mathbf{x})} = \nabla\boldsymbol{\chi}(\mathbf{x}) - \mathbf{F}(\mathbf{x}) = \mathbf{0}.$$

After the application of the Fourier transform, it reads as

$$\mathbf{P}(\mathbf{k}) - \boldsymbol{\Lambda}_0(\mathbf{x}) + \mathbb{D}\{\mathbf{F}(\mathbf{k}) - \boldsymbol{\chi}(\mathbf{k}) \otimes i\mathbf{k}\} = \mathbf{0},$$
$$\mathbf{A}^{-1}(\mathbf{k})\{\mathbb{D}\mathbf{F}(\mathbf{k}) - \boldsymbol{\Lambda}_0(\mathbf{x})\}i\mathbf{k} = \boldsymbol{\chi}(\mathbf{k}), \tag{28}$$
$$\boldsymbol{\chi}(\mathbf{k}) \otimes i\mathbf{k} - \mathbf{F}(\mathbf{k}) = \mathbf{0}$$

with the Lagrange multiplier field relative to the reference configuration as $\boldsymbol{\Lambda}_0(\mathbf{x}) = \mathbf{F}(\mathbf{x})\boldsymbol{\Lambda}(\mathbf{x})$. Eliminating $\boldsymbol{\chi}$ from Eqs. $(28)_{1,3}$ using Eq. $(28)_2$ gives the equilibrium deformation gradient field as the solution to

$$\mathcal{F}_{\mathrm{mix}}[\mathbf{F}(\mathbf{k}), \boldsymbol{\Lambda}_0(\mathbf{k})] := \begin{Bmatrix} \mathbf{P}(\mathbf{k}) - \boldsymbol{\Lambda}_0(\mathbf{k}) + \mathbb{D}(\mathbf{F}(\mathbf{k}) - \boldsymbol{\Gamma}(\mathbf{k})(\mathbb{D}\mathbf{F}(\mathbf{k}) - \boldsymbol{\Lambda}_0(\mathbf{k}))) \\ \mathbf{F}(\mathbf{k}) - \boldsymbol{\Gamma}(\mathbf{k})(\mathbb{D}\mathbf{F}(\mathbf{k}) - \boldsymbol{\Lambda}_0(\mathbf{k})) \end{Bmatrix} = \mathbf{0}. \tag{29}$$

The condition $\mathbf{F}(\mathbf{k}) - \boldsymbol{\Gamma}(\mathbf{k})(\mathbb{D}\mathbf{F}(\mathbf{k}) - \boldsymbol{\Lambda}_0(\mathbf{k})) = \mathbf{0}$ in Eq. (29) is necessary and sufficient to enforce both the compatibility of the deformation gradient field, given by $\mathbf{F}(\mathbf{k}) - \boldsymbol{\Gamma}(\mathbf{k})\mathbb{D}\mathbf{F}(\mathbf{k}) = \mathbf{0}$, and equilibrium of the Lagrange multiplier field, given by $\boldsymbol{\Gamma}(\mathbf{k})\boldsymbol{\Lambda}_0(\mathbf{k}) = \mathbf{0}$ (for details see [35]). The condition $\mathbf{P}(\mathbf{k}) - \boldsymbol{\Lambda}_0(\mathbf{k}) = \mathbf{0}$ enforces equilibrium of the stress field corresponding to $\mathbf{F}$.

2.7. Implementation

The hexahedral domain $\mathcal{B}_0$ with side lengths d_x, d_y, d_z is discretized into a regular grid of $N_x \times N_y \times N_z = N$ points with unit spacing. The solution field is approximated in the discrete Fourier space associated with this real space grid. For the transformation between real and Fourier space, the Fastest Fourier Transform in the West [44] developed by Frigo and Johnson [45] is used.

The choice of the reference stiffness $\mathbb{D}$ has a strong influence on stability and convergence rate as shown by Michel et al. [33]. In absence of an analytic expression for the large strain formulation the reference stiffness $\mathbb{D}$ is selected as

$$\mathbb{D} = \frac{\arg\max \left\|\mathrm{d}\mathbf{P}/\mathrm{d}\mathbf{F}(\mathbf{x})\right\|_{\mathrm{F}} + \arg\min \left\|\mathrm{d}\mathbf{P}/\mathrm{d}\mathbf{F}(\mathbf{x})\right\|_{\mathrm{F}}}{2}. \tag{30}$$

A collocation-based discretization approach at the grid points in real space is used to discretize Eq. (29). The static equilibrium condition is expressed in terms of the deformation gradient field and a rescaled polarization field, $\mathbf{F}_\tau(\mathbf{x}) := \mathbb{D}^{-1}(\mathbf{F}^{-1}(\mathbf{x})\boldsymbol{\Lambda}_0(\mathbf{x})) + \mathbf{F}(\mathbf{x})$. To get a well-conditioned system of equations, the inverse of the reference stiffness $\mathbb{D}^{-1}$ is used to scale the stress term in Eq. (29) resulting in the following expression:

$$\mathcal{F}_\tau[\mathbf{F}(\mathbf{x}), \mathbf{F}_\tau(\mathbf{x})] := \begin{Bmatrix} \mathbb{D}^{-1}(\mathbf{P}(\mathbf{x}) - \boldsymbol{\Lambda}_0(\mathbf{x})) + \beta\mathbf{F}(\mathbf{x}) - \\ -F^{-1}\left[\begin{cases} \boldsymbol{\Gamma}(\mathbf{k})(\beta\mathbb{D}\mathbf{F}(\mathbf{k}) - \alpha\boldsymbol{\Lambda}_0(\mathbf{k}), \text{ if } \mathbf{k} \neq \mathbf{0}, \\ \beta\mathbf{F}_{\mathrm{BC}}, \text{ if } \mathbf{k} = \mathbf{0} \end{cases}\right] \\ \beta\mathbf{F}(\mathbf{x}) - F^{-1}\left[\begin{cases} \boldsymbol{\Gamma}(\mathbf{k})(\beta\mathbb{D}\mathbf{F}(\mathbf{k}) - \alpha\boldsymbol{\Lambda}_0(\mathbf{k}), \\ \text{if } \mathbf{k} \neq \mathbf{0}, \\ \beta\mathbf{F}_{\mathrm{BC}}, \text{ if } \mathbf{k} = \mathbf{0} \end{cases}\right] \end{Bmatrix}. \tag{31}$$

The coefficients α and β with default value $\alpha = \beta = 1.0$ enable to weight the conditions for static equilibrium and strain compatibility. Their optimal choice depends on the problem type, e.g. the ratio of increased

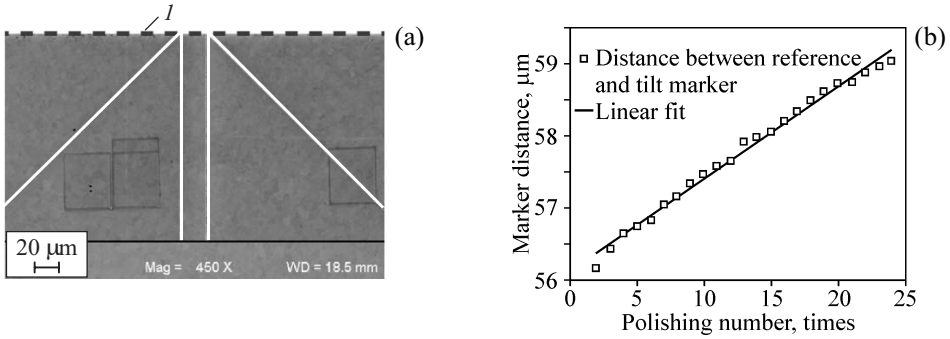

Fig. 1. The surface removal per polishing step is measured on markers perpendicular to the region of interest. (a) Markers on one of the parallel sides. Dashed line *1* indicates region of interest. (b) Surface removal per polishing step and linear fit.

or decreased stiffness compared to the average stiffness. A detailed study of their influence on the convergence rate is given by Moulinec and Silva [46] for a similar formulation in a small strain framework.

The desired deformation boundary condition $\mathbf{F}_{\mathrm{BC}}$ of the volume element is conveniently prescribed by setting $\Delta\mathbf{F}_{\mathrm{BC}} = \bar{\mathbf{F}} - \mathbf{F}_{\mathrm{BC}}$. This allows adjusting the deformation gradient such that a stress boundary condition is fulfilled component-wise as outlined by Eisenlohr et al. [38].

The nonlinear solution methods to solve the resulting systems of discretized equations are taken from PETSc [47] developed by Balay et al. [48]. The residual results from evaluating Eq. (31) at the grid points. Shanthraj et al. [39] compared three solution methods implemented in PETSc. The method showing the best performance in this benchmark, namely the nonlinear GMRES method [49], is used in this study.

2.8. Convergence Criteria

A solution is accepted if the stress field is equilibrated, the deformation gradient field is compatible and the macroscopic applied boundary conditions are fulfilled.

Using the differentiation property $F[\mathrm{d}f(x)/\mathrm{d}x] = i2\pi k\, f(k)$, the deviation from static equilibrium $\nabla\cdot\mathbf{P}$ and compatibility $\nabla\times\mathbf{F}$ can be calculated in Fourier space. Moreover, the root mean square (RMS) as a volume average is easily accessible as discussed in Eisenlohr et al. [38] in Fourier space. The corresponding equilibrium criterion reads:

$$\frac{\max(\varepsilon_{\mathrm{e,rel}}\left\|\bar{\mathbf{P}}\right\|_{\max}, \varepsilon_{\mathrm{e,abs}})}{m} \geq \mathrm{RMS}(\left\|\nabla\cdot\mathbf{P}(\mathbf{x})\right\|_2), \quad (32)$$

where $\varepsilon_{\mathrm{e,rel}}$ and $\varepsilon_{\mathrm{e,abs}}$ are the relative and absolute equilibrium tolerances. The expression to test for a compatible solution is

$$\frac{\max(\varepsilon_{\mathrm{c,rel}}\left\|\bar{\mathbf{F}} - \mathbf{I}\right\|_{\max}, \varepsilon_{\mathrm{c,abs}})}{m} \geq \mathrm{RMS}(\left\|\nabla\times\mathbf{F}(\mathbf{x})\right\|_{\mathrm{F}}), \quad (33)$$

where $\varepsilon_{\mathrm{c,rel}}$ and $\varepsilon_{\mathrm{c,abs}}$ are the relative and absolute compatibility tolerances.

The fulfillment of complementary macroscopic deformation gradient and stress boundary conditions is determined by

$$\max(\varepsilon_{\mathrm{BC,rel}}\left\|\bar{\mathbf{P}}\right\|_{\max}, \varepsilon_{\mathrm{BC,abs}}) \geq \left\|\Delta\mathbf{P}_{\mathrm{BC}}\right\|_{\max} \quad (34)$$

with $\Delta P_{\mathrm{BC}ij} = A_{ijkl}(F_{\mathrm{BC}} - \bar{F})_{kl}$, if $F_{\mathrm{BC}ij}$ is prescribed and $\Delta P_{\mathrm{BC}ij} = (P_{\mathrm{BC}} - \bar{P})_{ij}$, if $P_{\mathrm{BC}ij}$ prescribed and the relative and absolute tolerances $\varepsilon_{\mathrm{BC,rel}}$ and $\varepsilon_{\mathrm{BC,abs}}$.

3. MICROSTRUCTURE CHARACTERIZATION AND MODEL CREATION

The investigated material is a commercial dual phase steel grade containing the main alloy elements C (0.14 wt %), Mn (1.7 wt %), Si (0.24 wt %), Al (0.04 wt %), and Cr + Mo (0.56 wt %). The average grain size of ferrite is 5.0 μm and the martensite islands (each consisting of several laths with different crystallographic orientations) have on average a diameter of 0.5 μm.

In the following it is outlined how the 2D and 3D microstructural models are created from this material. Additionally, the parameters for the constitutive model and the loading boundary conditions are provided.

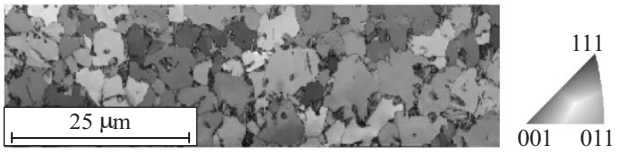

Fig. 2. Orientation map (colors according to inverse pole figure parallel to the normal direction) overlaid with the image quality (darker values indicate lower image quality, i.e. typically martensite). Rolling direction is horizontal.

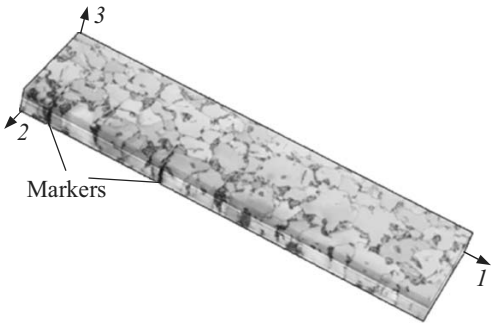

Fig. 3. 3D model constructed from 22 sections where the markers can clearly be seen. Color code displays image quality. A lower image quality (dark) indicates typically martensite. Arrow *1*—rolling direction, arrow *2*—transverse direction, arrow *3*—normal direction.

3.1. Sample Preparation and Microstructural Characterization

For obtaining a three-dimensional microstructure data set of the investigated material, a serial-sectioning approach that consists of multiple cycles of mechanical polishing and electron backscatter diffraction imaging [50] was employed. To this end, first a sample with two parallel sides of high surface quality was prepared by mechanical grinding and polishing. On each of those parallel surfaces, four marker lines were engraved by focused ion beam milling using a Zeiss Cross-Beam instrument (Fig. la). Two of these lines are parallel to each other and serve as a reference for magnification and positioning. The two other inclined lines have including angles of 45° with the reference lines and serve as markers to determine the polishing depth. In fact, after mounting the material and polishing the surface of the region of interest perpendicular to the marked surfaces, the marker lines appear as sharply peaked spikes at the edge of the sample. The change of distance between the depth markers and the reference markers then corresponds directly to the depth of polishing. In the present case the sample was warm mounted into conductive resin (Polyfast by Struers) into a cylindric mount of 25mm diameter.

For each measurement cycle, the sample was polished with silicon-oxide particle suspension produced by Struers at a pressure of 60 kPa for 4 min. This led to a removal of, in average, 0.13 μm per slice as displayed in Fig. 1b. Figure 1b moreover shows that the removal rate was approximately constant and varied by approximately 50 nm per slice. After every polishing step the sample was manually placed into a Zeiss XB 1540 high resolution scanning electron microscope. The sample was tilted to 70° and then manually moved to the original measurement position using the reference markers. Finally, an orientation map was taken using EBSD (OIM 6.x by EDAX/TSL using a Hikari camera) operating at 15 kV electron beam acceleration voltage. One of these acquired orientation maps is shown in Fig. 2.

In total, 22 slices, each sized 20×70 μm^2 (transverse × rolling direction) at an in-plane EBSD step size of 0.2 μm have been acquired. The CUBE software from Bruker [51] has been used to create a 3D model from all sections. The sample 20.0×70.0×2.86 μm^3 discretized by 351×100×22 = 772 200 points is shown in Fig. 3.

3.2. Model Creation

The model required for the crystal plasticity simulations to be conducted using the spectral solver can be directly created from the measured orientation data on the regular 3D voxel grid. However, due to the similar lattice constants, it is not directly possible to distinguish martensite and ferrite. The conventional approach of using the image quality as an indicator [5, 52] (which is lower for the heavily distorted rnartensitic crystals) is not applicable here as polishing and sample preparation introduced a substantial variation in image quality between the sections and even within one section. Therefore, the grain size was used to indicate whether a measured point pertains to the martensitic or to the ferritic phase. This approach is based on the ratio that (i) ferritic grains are 10 times larger than martesitic islands and (ii) in each martensite grain, several lath of distinct orientation can be identified as individual grains [52–55]. To this end, first each orientation map was cleaned using the features available within the TSL OIM software. After cleaning, a 3D model was created on which individual grains (i.e., in

Table 1. Constitutive parameters of ferrite and martensite used for the simulations taken from [5]

Property	C_{11}, GPa	C_{12}, GPa	C_{44}, GPa	$\dot{\gamma}_0$, s^{-1}	$\xi_{0,\{110\}}$, MPa	$\xi_{\infty,\{110\}}$, MPa	$\xi_{0,\{112\}}$, MPa	$\xi_{\infty,\{112\}}$, MPa	h_0, GPa	h_{km}	n	a
Ferrite	233.3	235.5	128.0	0.001	95	222	96	412	1	1	20	2.25
Martensite	417.4	242.4	211.1		406	873	457	971	563			

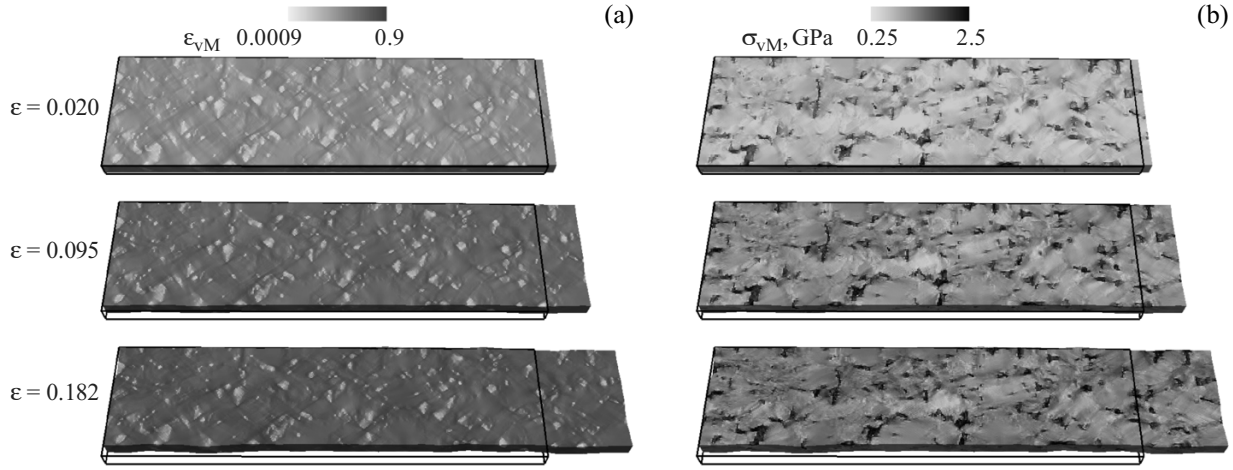

Fig. 4. Equivalent strain ε_{vM} (a) and stress σ_{vM} (b) at increasing strain level ε from top to bottom mapped onto the deformed configuration for the case of the 3D simulation. The surface shown is parallel to the normal plane. The black frame indicates the shape in the undeformed configuration. A logarithmic scale is used to for mapping the stress and strain values to the color bar in order to resolve details in both phases with their vastly differing mechanical properties.

the case of martensite, laths) have been identified using a tight tolerance angle of 3°. Now, all grains of a size smaller than 30 voxels have been considered as martensite. As a final step, all grains identified as martensite but consisting of only one voxel are considered and treated as a measurement artifact and are hence assigned with ferrite properties to avoid associated numerical artifacts. This leads to a volume fraction of 5.8% of martensite. A visual inspection of the segmentation achieved by this approach indicates a reasonable phase separation. However, few ferrite grains are erroneously detected to be martensite because they are smaller then the size threshold set for the phase separation. This issue on grain segmentation in three dimensions is directly related to the serial sectioning approach: The crystallographic orientations obtained from the individual EBSD measurements are mapped in a reference system relative to the assumed position of the sample on the microscope stage. Despite careful sample preparation and alignment, the position of the sample with respect to the EBSD detector differs between the individual measurements. Therefore, orientation differences significantly larger than the EBSD angular resolution of less than 2° (which is achieved in each individual map) appear between points belonging to the same grain but acquired in different sections. Moreover, at the surfaces of the measurement area where grains are cut off, detected grain sizes are smaller than in the volume and the wrong assignment occurs slightly more frequent than inside of the measurement block.

The three-dimensional model constructed from all 772 200 measured points has been mirrored in all three directions to avoid artifacts at the sample boundaries

Table 2. Minimum, mean, and maximum values of the equivalent stress and strain found in the 3D simulation at a global strain in loading direction of ε = 0.182

Phase	Equivalent stress σ_{vM}, GPa			Equivalent strain ε_{vM}		
	Minimum	Mean	Maximum	Minimum	Mean	Maximum
Ferrite	0.17	0.67	1.32	0.0026	0.2150	0.8648
Martensite	0.32	1.91	7.03	0.0008	0.0454	0.6905

Table 3. Minimum, mean, and maximum values of the equivalent stress and strain found in the 2D simulations at a global strain in loading direction of ε = 0.182

Phase	Equivalent stress σ_{vM}, GPa			Equivalent strain ε_{vM}		
	Minimum	Mean	Maximum	Minimum	Mean	Maximum
Ferrite	0.21	0.67	1.29	0.0322	0.2195	1.2503
Martensite	1.39	2.07	11.40	0.0291	0.0465	0.4851

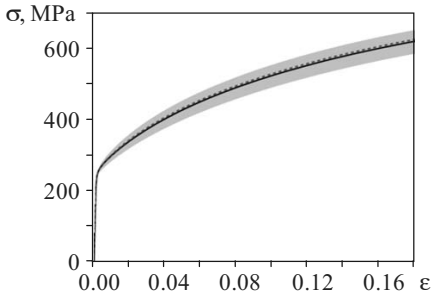

Fig. 5. Stress–strain response in loading direction obtained by the different simulations. The values of the 3D simulation is given by the solid line, the average value of the 2D simulations is given by the dashed line and the grey area indicates minimum and maximum values among all 2D simulations. Cauchy stress and true strain are computed from $\overline{\mathbf{F}}$ and $\overline{\mathbf{P}}$.

introduced by the periodic repetition due to the approximation of the deformation gradient and stress fields by a Fourier series. Additionally, from each of the original 22 slices, a 2D model (still mirrored in both in-plane directions) is created to investigate the influence of a simplified columnar grain structure on the stress and strain partitioning in the spirit of Diehl et al. [12]. The martensite volume fraction ranges from 1.8 to 8.9% in the 2D models.

Material parameters that were before fitted to a similar material by Tasan et al. [5] are used in this study (Table 1).

Uniaxial tensile loading along the rolling direction at an engineering strain rate of 1×10^{-3} s^{-1} was applied for 200 s in 400 increments, i.e. a final true strain of $\varepsilon = 0.182$ was reached. This load case reflects the situation in a tensile test and has little deformation constraints compared to, e.g., plane stress loading. It should be noted that the values are prescribed as volume average for a periodically repeated body (compare Sect. 2.3) and hence differ from typical (nonperiodic) boundary conditions used in finite element analysis.

4. RESULTS

4.1. Three-Dimensional Model

The spatial distribution of the equivalent (von Mises) strain ε_{vM} and stress σ_{vM} is shown in Fig. 4 for three different loading states, i.e. at $\varepsilon = 0.020$, 0.095, and 0.182, where ε denotes the logarithmic (true) strain along loading direction. A significant stress and strain partitioning among the phases can be seen at each load level. The spatial distribution over time, i.e. from top to bottom in Fig. 4, is largely constant as the same locations at $\varepsilon = 0.020$, 0.095, and 0.182 can be identified as being low respectively high stressed/strained. Among different ferrite grains and within the same grain, a large variation in stress can be observed at all three load levels (Fig. 4b). The extreme values of stress and strain at $\varepsilon = 0.182$ in both phases are given together with the corresponding mean value in Table 2. As expected, the stress in martensite is much higher than in ferrite while the opposite holds for the strain. The strain in martensite between different regions differs by more than one order of magnitude and the stress by almost three orders of magnitude. In ferrite, the differences are slightly lower, i.e. by almost one order of magnitude in strain and by more than two orders of magnitude in stress.

4.2. Comparison between the Three-Dimensional Model and the Two-Dimensional Models

The global stress–strain curves in terms of the average Cauchy stress and logarithmic strain in loading

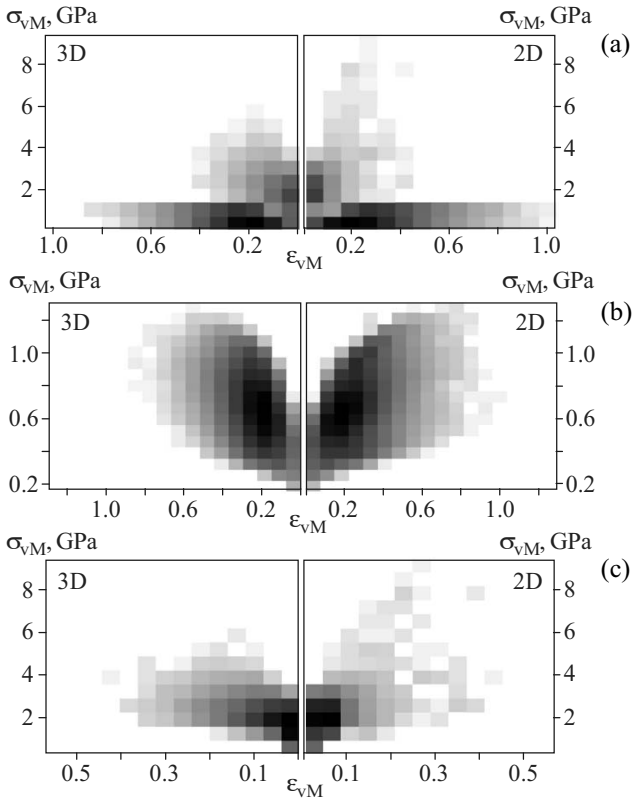

Fig. 6. Probability density maps showing the correlation between equivalent stress and strain within the 3D simulation (left) and all 2D simulations (right). Darker value indicates higher probability to find the stress–strain correlation. Ferrite and martensite (a), ferrite only (b) and martensite only (c).

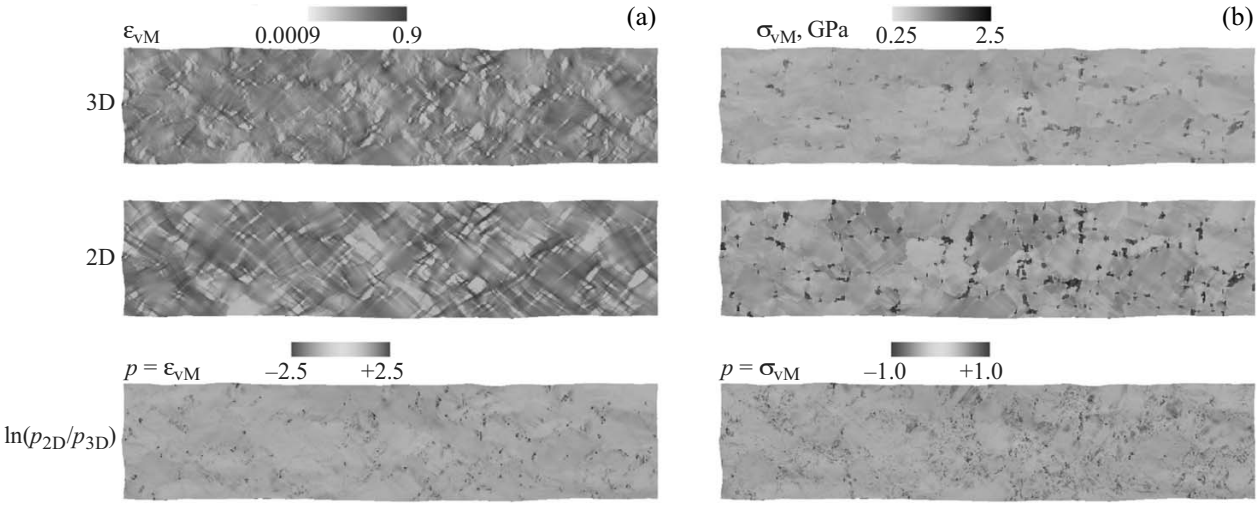

Fig. 7. Equivalent strain ε_{vM} (a) and stress σ_{vM} (b) in a section of the 3D microstructure (top) and in the corresponding 2D microstructure (middle) and the logarithmic of the ratio between them (bottom) mapped onto the deformed configuration of the 3D simulation ($\varepsilon = 0.182$). The section shown is parallel to the normal plane. A logarithmic scale is used for mapping the stress and strain values in order to resolve details in both phases with their vastly differing mechanical properties.

direction for the 3D simulation together with the average and the extrema of the 2D individual simulations are given in Fig. 5. The average response of all 2D simulations, i.e. considering all voxel in the 3D volume and doing individual simulations for each section, is almost the same as the response for the full model. A difference between the softest and the stiffest section of approximately 70 MPa can be observed.

Table 3 gives the minimum, mean, and maximum values of the equivalent strain and stress obtained by the 2D simulations for a global strain of $\varepsilon = 0.182$. A comparison of the stress values (Table 3) to the results obtained from the 3D simulation (given in Table 2) reveals that the 2D simulation predicts a more homogeneous distribution around the same average in ferrite while minimum, average, and maximum values in the martensitic phase are substantially higher in the 2D situation than in their 3D counterpart. The mean values of the equivalent strain show no significant difference between the 2D assumption and the 3D model (compare Table 3 with Table 2). A wider distribution of the strain values in martensite results from the 3D simulation while in ferrite the minimum and maximum values are significantly higher in the 2D case.

In Fig. 6, probability density maps ("heat maps") are given for comparison of the stress-strain partitioning in the 3D simulation (left) to the sum of all 2D simulations (right). More specifically, Fig. 6a displays the probability density of equivalent strain and stress for ferrite and martensite together. Fig. 6b shows it for ferrite only, and Fig. 6c for martensite only. A bipartitioned distribution can be seen in Fig. 6a: At the bottom (low stress) the values belonging to the ferrite are located and at low strains (horizontal center) the values of the martensitic phase. This representation confirms the findings that the 2D situation leads to higher strain and stress values in martensite while the ferrite is more strained, but stays at a similar stress level. Figures 6b and 6c showing the heat maps for both phases individually allow to investigate behavior of martensite and ferrite more closely. From Fig. 6b the significant different stress levels in ferrite can be accessed. Figure 6c reveals that in the 2D simulations a substantial share of martensite shows stress values above the maximum value found in the 3D simulation.

A point-to-point comparison of the equivalent strain and stress maps for one section in the center of the 3D microstructure is given in Fig. 7. It can be observed that the stress in martensite is higher in the 2D situation, a trend perceived also from the comparison of Table 3 with Table 2. To visualize the differences between the results obtained by both simulations, first the ratio between the shown values is computed followed by taking the natural logarithm of it: $\ln(p_{2D}/p_{3D})$ for $p \in \sigma_{vM}, \varepsilon_{vM}$. This measure is motivated from the true (logarithmic) strain measure. Its desired property is the asymptotic behavior, $\lim_{p_{2D}\to\pm\infty} \ln(p_{2D}/p_{3D}) = \pm\infty$ in contrast to the relative difference which has lower bound of –1 and upper bound of $+\infty$. Hence, this measure is better suited then a "standard" relative difference when large deviations to both, lower and higher

values, occur. Maps showing the obtained values for stress and strain are given in the bottom row of Fig. 7. It can be seen that the relative differences in strain are especially large in or in the vicinity of martensite, while the largest relative stress difference is often found in ferrite.

5. DISCUSSION

The results presented above clearly emphasize the severe strain and stress partitioning occurring in dual phase steels caused by the very different mechanical behavior of martensite and ferrite. The magnitude and pattern of the partitioning depends on details such as martensite shape and distribution, crystallographic orientation and misorientation that have been included into the simulation by using an experimentally characterized microstructure as input data.

The global stress–strain response of a 3D model and the 2D microstructures built from this 3D models differs only slightly. This is especially astonishing as the martensite volume fraction of the individual sections differs significantly from their average given by the 3D model. In contrast, the local response is vastly changed when a 2D section is used alone compared to embedding it into the experimentally obtained neighborhood. In fact, the 2D simulations show strain hot spots which are up to 11 times higher in strain and up to 3 times higher in stress than the same positions in the 3D simulations. The reason for this is that the columnar structure of the 2D simulation does not allow for relaxation or support through different deformation paths above or below the observed structure. As a consequence all strain paths follow a 2D-pattern resulting in the observed intense shear patterns in the 2D simulations. In contrast, the 3D simulations allow strain paths in 3 dimensions, thus resulting in lower stress and strain concentrations. These observations show that the analysis of local strain features, for example for the understanding of crack nucleation, imperatively need 3D calculations with realistic microstructure input.

6. CONCLUSION AND OUTLOOK

A dual phase steel microstructure model based directly on a data set obtained by a 3D EBSD characterization approach has been utilized for a simulation study using a crystal plasticity approach in combination with a fast spectral solver included in the free and open source software DAMASK. The microstructural model, by including details such as martensite shape and distribution, crystallographic orientation and misorientation, allows to investigate stress and strain partitioning without significant simplifications. The proposed modeling method and the approach for obtaining the microstructure by serial sectioning are therefore a promising route for the efficient investigation of stress and strain partitioning in dual phase steels and other materials with complex microstructures.

2D models, assuming a columnar grain structure, have been used to investigate the influence of this simplification. In agreement with Diehl et al. [12] it is clearly shown how important full 3D microstructures are for capturing the details of stress and strain partitioning in dual phase steels for the investigated loading conditions. While no large effect on the global response could be found, the local stress and strain values differ quantitatively and qualitatively when a 2D model is used instead of a 3D model. Especially for simulations tackling the question of damage initiation in dual phase steels (for damage models implemented in DAMASK see [57]), 2D modelling is therefore an unsuitable and erroneous approach: As these damage models predict damage based on the local stress or strain response, relying on values that are off by a factor of up to 3 for the stress and by a factor of up to 11 for the strain when employing a 2D model would in most cases result in entirely incorrect simulation results and conclusions.

For building the model of dual phase steel, the distinct separation of both phases remains a challenge. It can be expected that replacing the manual serial sectioning approach presented here by an automated system will help to solve this problem. First, a more reproducible surface preparation will restore the possibility to use the image quality as a phase indicator. Second, a more exact placement of the sample in the EBSD system will reduce the deviations in measured crystallographic orientation between different acquisition runs. Combining both indicators, i.e. grain size and (grain average) image quality into one algorithm should then allow to reliably separate martensite and ferrite. Moreover, an automated system will reduce experimental efforts and enable to investigate larger volumes and improve statistical confidence.

ACKNOWLEDGMENTS

M. Diehl acknowledges the funding of the TCMPrecipSteel project in the framework of the SPP 1713 (Strong coupling of thermo-chemical and thermo-mechanical states in applied materials) by the Deutsche Forschungsgemein-schaft (DFG).

REFERENCES

1. Tasan, C.C., Diehl, M., Yan, D., Bechtold, M., Roters, F., Schemmann, L., Zheng, C., Peranio, N., Ponge, D., Koyama, M., Tsuzaki, K., and Raabe, D., An Overview of Dual-Phase Steels: Advances in Microstructure-Oriented Processing and Micromechanically Gided Design, *Annu. Rev. Mater. Res*., 2015, vol. 45, pp. 391–431.
2. Karlsson, B. and Sundström, B.O., Inhomogeneity in Plastic Deformation of Two-Phase Steels, *Mater. Sci. Eng*., 1974, vol. 16(1–2), pp. 161–168.
3. Kadkhodapour, J., Butz, A., Ziaei-Rad, S., and Schmauder, S., A Micromechanical Study on Failure Initiation of Dual Phase Steels under Tension Using Single Crystal Plasticity Model, *Int. J. Plasticity*, 2011, vol. 27(7), pp. 1103–1125.
4. Tasan, C.C., Hoefnagels, J.P.M., Diehl, M., Yan, D., Roters, F., and Raabe, D., Strain Localization and Damage in Dual Phase Steels Investigated by Coupled In-situ Deformation Experiments–Crystal Plasticity Simulations, *Int. J. Plasticity*, 2014, vol. 63, pp. 198–210.
5. Tasan, C.C., Diehl, M., Yan, D., Zambaldi, C., Shanthraj, P., Roters, F., and Raabe, D., Integrated Experimental-Numerical Analysis of Stress and Strain Partitioning in Multi-Phase Alloys, *Acta Mater*., 2014, vol. 81, pp. 386–400.
6. Scherff, F., Goldschmidt, F., Scholl, S., and Diebels, S., High-Resolution Simulation of Microstructures in Dual-Phase Steel, *PAMM*, 2016, vol. 16(1), pp. 391–392.
7. Uthaisangsuk, V., Prahl, U., and Bleck, W., Stretch-Flangeability Characterization of Multiphase Steel Using a Microstructure Based Failure Modeling, *Comp. Mater. Sci*., 2009, vol. 45(3), pp. 617–623.
8. Fillafer, A., Krempaszky, C., and Werner, E., On Strain Partitioning and Micro-Damage Behavior of Dual-Phase Steels, *Mater. Sci. Eng. A*, 2014, vol. 614, pp. 180–192.
9. Scheunemann, L., Balzani, D., Brands, D., Schröder, J., and Raabe, D., Statistically Similar RVE Construction Based on 3D Dual-Phase Steel Microstructures, *Proc. 5th Int. Conf. Structural Engineering, Mechanics and Computation*, Boca Raton: CRC Press, 2013, pp. 411–416.
10. Brands, D., Balzani, D., Scheunemann, L., Schröder, J., Richter, H., and Raabe, D., Computational Modeling of Dual-Phase Steels Based on Representative Three-Dimensional Microstructures Obtained from EBSD Data, *Arch. Appl. Mech*., 2016, vol. 86(3), pp. 575–598.
11. Woo, W., Em, V.T., Kim, E-Y, Han, S.H., Han, Y.S., and Choi, S-H, Stress–Strain Relationship between Ferrite and Martensite in a Dual-Phase Steel Studied by in Situ Neutron Diffraction and Crystal Plasticity Theories, *Acta Mater*., 2012, vol. 60(20), pp. 6972–6981.
12. Diehl, M., Shanthraj, P., Eisenlohr, P., and Roters, F., Neighborhood Influences on Stress and Strain Partitioning in Dual-Phase Microstructures. An Investigation on Synthetic Polycrystals with a Robust Spectral-Based Numerical Method, *Meccanica*, 2016, vol. 51(2), pp. 429–441.
13. Pagenkopf, J., Butz, A., Wenk, M., and Helm, D., Virtual Testing of Dual-Phase Steels: Effect of Martensite Morphology on Plastic Flow Behavior, *Mater. Sci. Eng. A*, 2016, vol. 674, pp. 672–686.
14. Zeghadi, A., N'guyen, F., Forest, S., Gourgues, A-F, and Bouaziz, O., Ensemble Averaging Stress–Strain Fields in Polycrystalline Aggregates with a Constrained Surface Microstructure. Part 1: Anisotropic Elastic Behavior, *Philos. Mag.*, 2007, vol. 87(8–9), pp. 1401–1424.
15. Zeghadi, A., Forest, S., Gourgues, A.-F., and Bouaziz, O., Ensemble Averaging Stress–Strain Fields in Polycrystalline Aggregates with a Constrained Surface Microstructure. Part 2: Crystal Plasticity, *Philos. Mag*., vol. 87(8–9).
16. Roters, F., Eisenlohr, P., Kords, C., Tjahjanto, D.D., Diehl, M., and Raabe, D., DAMASK: the Dusseldorf Advanced Material Simulation Kit for Studying Crystal Plasticity Using an FE Based or a Spectral Numerical Solver, *Proc. IUTAM: From Microstructure to Macroscale Properties*, Cazacu, O., Ed., Amsterdam: Elsevier, 2012, vol. 3, pp. 3–10.
17. Reina, C. and Conti, S., Kinematic Description of Crystal Plasticity in the Finite Kinematic Framework: A Micromechanical Understanding of $F = F_eF_p$, *J. Mech. Phys. Solids*, 2014, vol. 67, pp. 40–61.
18. Roters, F., Eisenlohr, P., Bieler, T.R., and Raabe, D., *Crystal Plasticity Finite Element Methods in Materials Science and Engineering*, Weinheim: Wiley-VCH, 2010.
19. Kords, C., *On the Role of Dislocation Transport in the Constitutive Description of Crystal Plasticity: PhD Thesis*, Berlin: RWTH Aachen, 2013. http://darwin.bth.rwth-aachen.de/opus3/volltexte/2014/4862
20. Hutchinson, J.W., Bounds and Self-Consistent Estimates for Creep of Polycrystalline Materials, *Proc. R. Soc. A*, 1976, vol. 348, pp. 101–127.
21. Gottstein, G., *Physical Foundations of Material Science*, Berlin: Springer, 2004.
22. Gröger, R. and Vitek, V., Breakdown of the Schmid Law in BCC Molybdenum Related to the Effect of Shear Stress Perpendicular to the Slip Direction, *Mat. Sci. Forum*, 2005, vol. 482, pp. 123–126.
23. Moulinec, H. and Suquet, P., A Fast Numerical Method for Computing the Linear and Nonlinear Properties of Composites, *Comptes Rendus de l'Academie des Sciences. Ser. II. Mecanique, Physique, Chimie, Astronomie*, 1994, vol. 318, pp. 1417–1423.
24. Schneider, M., Ospald, F., and Kabel, M., Computational Homogenization of Elasticity on a Staggered Grid, *Int. J. Numer. Meth. Eng*., 2015, vol. 105(9), pp. 693–720.
25. Kabel, M., Fliegener, S., and Schneider, M., Mixed Boundary Conditions for FFT-Based Homogenization at Finite Strains, *Comp. Mater. Sci*., 2016, vol. 57(2), pp. 193–210.
26. Zeman, J., de Geus, T.W.J., Vondřejc, J., Peerlings, R.H.J., and Geers, M.G.D., A Finite Element Perspective on Non-Linear FFT-Based Micromechanical Simulations, *Int. J. Numer. Meth. Eng*., 2017. doi 10.1002/nme.5481
27. Lebensohn, R.A., N-Site Modeling of a 3D Viscoplastic Polycrystal Using Fast Fourier Transform, *Acta Mater*., 2001, vol. 49(14), pp. 2723–2737.
28. Lebensohn, R.A., Castelnau, O., Brenner, R., and Gilormini, P., Study of the Antiplane Deformation of Linear 2D Polycrystals with Different Microstructures, *Int. J. Solids. Struct*., 2005, vol. 42(20), pp. 5441–5459.

29. Lefebvre, G., Sinclair, C.W., Lebensohn, R.A., and Mithieux, J.-D., Accounting for Local Interactions in the Prediction of Roping of Ferritic Stainless Steel Sheets, *Model. Simul. Mater. Sci. Eng*., 2012, vol. 20(2), p. 024008.
30. Lebensohn, R.A., Kanjarla, A.K., and Eisenlohr, P., An Elasto-Viscoplastic Formulation Based on Fast Fourier Transforms for the Prediction of Micromechanical Fields in Polycrystalline Materials, *Int. J. Plasticity*, 2012, vol. 32–33, pp. 59–69.
31. Suquet, P., Moulinec, H., Castelnau, O., Montagnat, M., Lahellec, N., Grennerat, F., Duval, P., and Brenner, R., Mult-Scale Modeling of the Mechanical Behavior of Polycrystalline Ice under Transient Creep, *Procedia IUTAM*, 2012, vol. 3, pp. 76–90.
32. Grennerat, F., Montagnat, M., Castelnau, O., Vacher, P., Moulinec, H., Suquet, P., and Duval, P., Experimental Characterization of the Intragranular Strain Field in Columnar Ice during Transient Creep, *Acta Mater*., 2012, vol. 60(8), pp. 3655–3666.
33. Michel, J.C., Moulinec, H., and Suquet, P., A Computational Scheme for Linear and Non-Linear Composites with Arbitrary Phase Contrast, *Int. J. Numer. Meth. Eng*., 2001, vol. 52(12), pp. 139–160.
34. Eyre, D.J. and Milton, G.W., A Fast Numerical Scheme for Computing the Response of Composites Using Grid Refinement, *Eur. Phys. J. Appl. Phys*., 1999, vol. 6(1), pp. 41–47.
35. Monchiet, V. and Bonnet, G., A Polarization-Based FFT Iterative Scheme for Computing the Effective Properties of Elastic Composites with Arbitrary Contrast, *Int. J. Numer. Meth. Eng*., 2012, vol. 89(11), pp. 1419–1436.
36. Zeman, J., Vondřejc, J., Novák, J., and Marek, I., Accelerating a FFT-Based Solver for Numerical Homogenization of Periodic Media by Conjugate Gradients, *J. Comput. Phys*., 2010, vol. 229(21), pp. 8065–8071.
37. Brisard, S. and Dormieux, L., FFT-Based Methods for the Mechanics of Composites: A General Variational Framework, *Comp. Mater. Sci*., 2010, vol. 49(3), pp. 663–671.
38. Eisenlohr, P., Diehl, M., Lebensohn, R.A., and Roters, F., A Spectral Method Solution to Crystal Elasto-Viscoplasticity at Finite Strains, *Int. J. Plasticity*, 2013, vol. 46, pp. 37–53.
39. Shanthraj, P., Eisenlohr, P., Diehl, M., and Roters, F., Numerically Robust Spectral Methods for Crystal Plasticity Simulations of Heterogeneous Materials, *Int. J. Plasticity*, 2015, vol. 66, pp. 31–45.
40. Lahellec, N., Michel, J.C., Moulinec, H., and Suquet, P., Analysis of Inhomogeneous Materials at Large Strains Using Fast Fourier Transforms, *Solid Mechanics and Its Applications: IUTAM Symposium on Computational Mechanics of Solid Materials at Large Strains*, Miehe, C., Ed., Dordrecht: Kluwer Academic Publishers, 2001, vol. 108, pp. 247–258.
41. Mura, T., *Micromechanics of Defects in Solids*, Dordrecht: Martinus Nijhoff Publishers, 1987.
42. Michel, J.C., Moulinec, H., and Suquet, P., A Computational Method Based on Augmented Lagrangians and Fast Fourier Transforms for Composites with High Contrast, *Comput. Model. Eng. Sci*., 2000, vol. 1(2), pp. 79–88.
43. *Augmented Lagrangian Methods: Applications to the Numerical Solution of Boundary-Value Problems*, Fortin, M. and Glowinski, R., Eds., 1983.
44. Frigo, M. and Johnson, S.G., *FFTW*, 2014. http://www.fftw.org
45. Frigo, M. and Johnson, S.G., The Design and Implementation of FFTW3, *Proc. IEEE*, 2005, vol. 93(2), pp. 216–231.
46. Moulinec, H. and Silva, F., Comparison of Three Accelerated FFT-Based Schemes for Computing the Mechanical Response of Composite Materials, *Int. J. Numer. Meth. Eng*., 2014, vol. 97(13), pp. 960–985.
47. *PETSc Team*, 2015. http://www.mcs.anl.gov/petsc
48. Balay, S., Brown, J., Buschelman, K., Eijkhout, V., Gropp, W.D., Kaushik, D., Knepley, M.G., McInnes, L.C., Smith, B.F., and Zhang, H., *PETSc Users Manual: Technical Report*, 2013.
49. Oosterlee, C.W. and Washio, T., Krylov Subspace Acceleration of Nonlinear Multigrid with Application to Recirculating Flows, *SIAM J. Sci. Comput*., 2000, vol. 21(5), pp. 1670–1690.
50. Zaefferer, S., Wright, S.I., and Raabe, D., Three-Dimensional Orientation Microscopy in a Focused Ion Beam-Scanning Electron Microscope: A New Dimension of Microstructure Characterization, *Metall. Mater. Trans. A*, 2008, vol. 39(2), pp. 374–389.
51. Konijnenberg, P.J., Zaefferer, S., Lee, S.B., Rollett, A.D., Rohrer, G.S., and Raabe, D., Advanced Methods and Tools for Reconstruction and Analysis of Grain Boundaries from 3D-EBSD Data Sets, *Mat. Sci. Forum*, 2011, vol. 702–703, pp. 475–478.
52. Schemmann, L., Zaefferer, S., Raabe, D., Friedel, F., and Mattissen, D., Alloying Effects on Microstructure Formation of Dual Phase Steels, *Acta Mater*., 2015, vol. 95, pp. 386–398.
53. Morito, S., Tanaka, H., Konishi, R., Furuhara, T., and Maki, T., The Morphology and Crystallography of Lath Martensite in Fe-C Alloys, *Acta Mater*., 2003, vol. 51(6), pp. 1789–1799.
54. Calcagnotto, M., Adachi, Y., Ponge, D., and Raabe, D., Deformation and Fracture Mechanisms in Fine- and Ultrafinegrained Ferrite/Martensite Dual-Phase Steels and the Effect of Aging, *Acta Mater*., 2011, vol. 59(2), pp. 658–670.
55. Yan, D., Tasan, C.C., and Raabe, D., High Resolution in Situ Mapping of Microstrain and Microstructure Evolution Reveals Damage Resistance Criteria in Dual Phase Steels, *Acta Mater*., 2015, vol. 96, pp. 399–409.
56. Shanthraj, P., Sharma, L., Svendsen, B., Roters, F., and Raabe, D., A Phase Field Model for Damage in Elasto-Viscoplastic Materials, *Comput. Meth. Appl. Mech. Eng*., 2016, vol. 312, pp. 167–185.
57. Shanthraj, P., Svendsen, B., Sharma, L., Roters, F., and Raabe, D., Elasto-Viscoplastic Phase Field Modeling of Anisotropic Cleavage Fracture, *J. Mech. Phys. Solids*, 2017, vol. 99, pp. 19–34.